

# Reversing the Catalytic Selectivity of Single-Atom Ru via Support Amorphization

Junyi Du,<sup>△</sup> Yan Huang,<sup>△</sup> Zixiang Huang,<sup>△</sup> Geng Wu, Bei Wu, Xiao Han, Cai Chen, Xusheng Zheng, Peixin Cui, Yuen Wu, Jun Jiang,\* and Xun Hong\*



Cite This: *JACS Au* 2022, 2, 1078–1083



Read Online

ACCESS |



Metrics & More



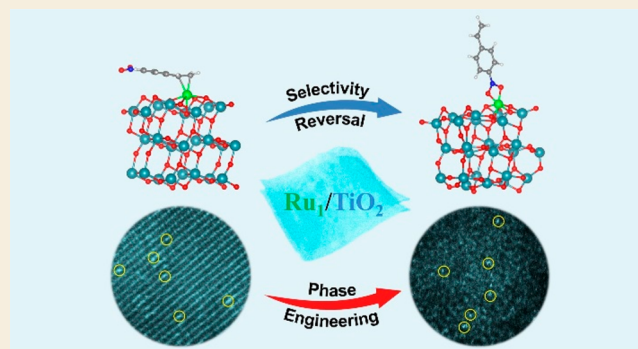
Article Recommendations



Supporting Information

**ABSTRACT:** Supported single-atom catalysts (SACs), with the extremely homogenized active sites could achieve high hydrogenation selectivity toward one of the functional groups coexisting in the reactant molecule. However, as to the target group, the control of selective recognition and activation by SACs still remains a challenge. Herein, the phase engineering of the support is adopted to control the chemo-recognition behavior of SACs in selective hydrogenation. Single-atom Ru on amorphous porous ultrathin TiO<sub>2</sub> nanosheets (Ru<sub>1</sub>/a-TiO<sub>2</sub>) is constructed, in which Ru is more positively charged than that in the crystalline counterpart (Ru<sub>1</sub>/c-TiO<sub>2</sub>). Moreover, in the nitro/vinyl selective hydrogenation process, Ru<sub>1</sub>/a-TiO<sub>2</sub> shows superior nitro selectivity, opposite to the vinyl selectivity of Ru<sub>1</sub>/c-TiO<sub>2</sub>. Density functional theory calculations for single-atom Ru of different charge states show that the reactant adsorption configuration could be inverted in the amorphous TiO<sub>2</sub>, accounting for the chemo-recognition behavior controlled by the phase of support.

**KEYWORDS:** single-atom catalysis, phase engineering, amorphous materials, hydrogenation, chemoselectivity



Selective hydrogenation is highly desirable in biomass conversions and fine chemical industries but difficult to realize due to the intramolecular competitive activation of different functional groups.<sup>1–4</sup> A typical example is the nitro selective hydrogenation of 4-nitrostyrene to afford 4-aminostyrene, an important building block molecule for various chemical products, like poly(4-aminostyrene) (PAS) and its copolymers.<sup>5,6</sup> The adsorption strength and configuration of the reactant molecule, which determines the reaction pathways and thus the selectivity, is dependent on the geometric and electronic structure of the active sites in the supported metal catalyst.<sup>7–9</sup> However, more than one type of active site may be coexisting in the catalyst due to the metal sizes, exposed facets, and metal–support interfaces.<sup>10–12</sup> To avoid multiple adsorption modes, thereby only activating one group, single-atom catalysts (SACs), featured by homogenizing the supported metal at atomic level, have been proved to be effective in recent years.<sup>13,14</sup> For example, in the selective hydrogenation of C–OH versus C=O, single-atom Pt on defective Nb<sub>2</sub>O<sub>5</sub> exhibited superior selectivity, but opposite to the Pt nanoparticles.<sup>15</sup> In general, as to a group intended to be hydrogenated in a reactant, it is critical for SACs to recognize a specific group from the coexisting groups (i.e., chemo-recognition) for targeted activation. Otherwise, other groups may be selectively hydrogenated instead. However, the control

of chemo-recognition for SACs in selective hydrogenation still remains a challenge.

To this end, the support is required to be optimized to regulate the chemical environment of the single metal atoms. Indeed, the change in the electronic metal–support interactions (EMSI) could lead to different adsorption behaviors of the reactant molecule on SACs.<sup>16,17</sup> Generally, the single-atom sites could be modulated through the EMSI effect by adjusting the elemental composition of the support, such as choosing different transition metal oxides or expanding the support to transition metal nitrides/carbides/dichalcogenides.<sup>18–21</sup> In this work, the phase engineering of the metal-oxide support is adopted to alter the status of the single-atom metal sites. As the opposite of the crystalline phase, the amorphous phase offers disordered adjacent atoms for the single-atom metal,<sup>22,23</sup> which may distinctively change the active site geometrically and electronically for different types of chemo-recognition. Herein, single-atom Ru on amorphous TiO<sub>2</sub> mesoporous ultrathin nanosheets (denoted as Ru<sub>1</sub>/a-

Received: March 25, 2022

Revised: May 4, 2022

Accepted: May 4, 2022

Published: May 6, 2022



TiO<sub>2</sub>) was synthesized in one step. The amorphous phase of TiO<sub>2</sub> was found to be crucial for modulating the charge state of Ru, which in turn affected its selectivity in the nitro/vinyl hydrogenation process.

The amorphous Ru<sub>1</sub>/a-TiO<sub>2</sub> was prepared in one step by directly annealing the mixture of ruthenium and titanium acetylacetonates ( $m_1/m_2 \sim 1:100$ ) with KBr at 300 °C under air, followed by removing the salt-template with water. Inductively coupled plasma optical emission spectroscopy (ICP-OES) shows that the Ru content of Ru<sub>1</sub>/a-TiO<sub>2</sub> is about 0.6 wt %. Powder X-ray diffraction (PXRD) confirms the amorphous phase and excludes the existence of Ru particles (PDF #06-0663) (Figure S1). Transmission electron microscopy (TEM) and scanning electron microscopy (SEM) exhibit a porous ultrathin nanosheet morphology (Figures 1A and S2).

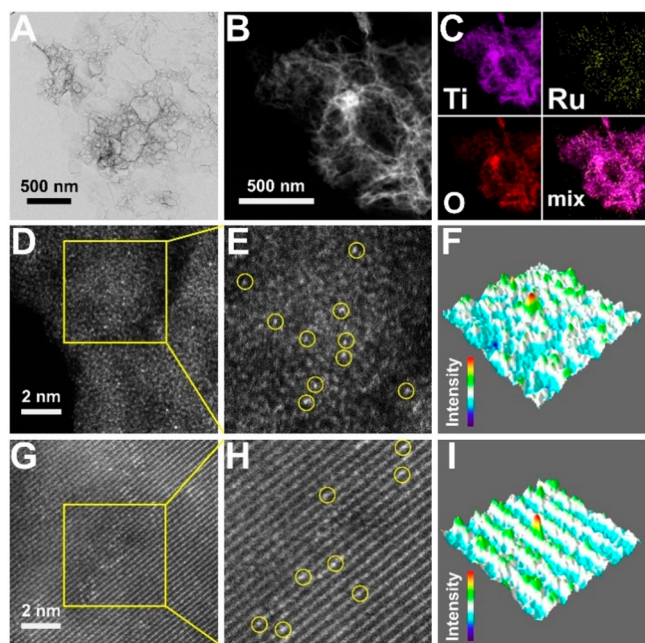


**Figure 1.** Structural and morphological characterizations of Ru<sub>1</sub>/a-TiO<sub>2</sub> and Ru<sub>1</sub>/c-TiO<sub>2</sub>. (A) TEM and (B) HAADF-STEM images of Ru<sub>1</sub>/a-TiO<sub>2</sub> and (C) corresponding elemental mapping. AC-HAADF-STEM and surface intensity profile images of (D–F) Ru<sub>1</sub>/a-TiO<sub>2</sub> and (G–I) Ru<sub>1</sub>/c-TiO<sub>2</sub>.

The thickness is about 7 nm according to the atomic force microscopy (AFM) analysis (Figure S3). From the high-angle annular dark-field scanning transmission electron microscopy (HAADF-STEM) image, the sponge-like porous structure of the nanosheets is clearly observed (Figure 1B). Energy dispersive X-ray (EDX) mappings illustrate that the Ru atoms are homogeneously distributed throughout the nanosheets (Figures 1C and S4). N<sub>2</sub> sorption tests further reveal the mesoporous feature (Figure S5) with a high specific surface area of 102 m<sup>2</sup>/g (Figure S6). The crystalline counterpart Ru<sub>1</sub>/c-TiO<sub>2</sub> was fabricated by reheating Ru<sub>1</sub>/a-TiO<sub>2</sub> at 450 °C. Although the ultrathin porous structure and the uniform elemental distribution are well maintained in Ru<sub>1</sub>/c-TiO<sub>2</sub> (Figures S2–S7), XRD suggests a typical anatase phase (PDF#21-1272) (Figure S1).

Aberration-corrected (AC) HAADF-STEM reveals the atomically dispersed Ru on amorphous TiO<sub>2</sub> at a relatively high contrast (Figure 1D and E). Figure 1F shows the surface

intensity profile of a typical isolated Ru atom among the disordered matrix. In contrast, an ordered atomic arrangement is manifested by Ru<sub>1</sub>/c-TiO<sub>2</sub> (Figure 1G and H), in which Ru atoms are anchored individually in the consecutive lattice fringes (Figure 1I). Furthermore, wavelet transforms (WT) of Ru K-edge extended X-ray absorption fine structure (EXAFS) spectra demonstrate no intensity maximum corresponding to metallic Ru–Ru for both Ru<sub>1</sub>/a-TiO<sub>2</sub> and Ru<sub>1</sub>/c-TiO<sub>2</sub> (Figure S8), confirming the atomic dispersion of Ru.

In the X-ray absorption near-edge structure (XANES) spectra for Ru K-edge, Ru in Ru<sub>1</sub>/a-TiO<sub>2</sub> and Ru<sub>1</sub>/c-TiO<sub>2</sub> both illustrates cationic properties, but the former is far more positively charged than the latter (Figure 2A). Since the Ru K-

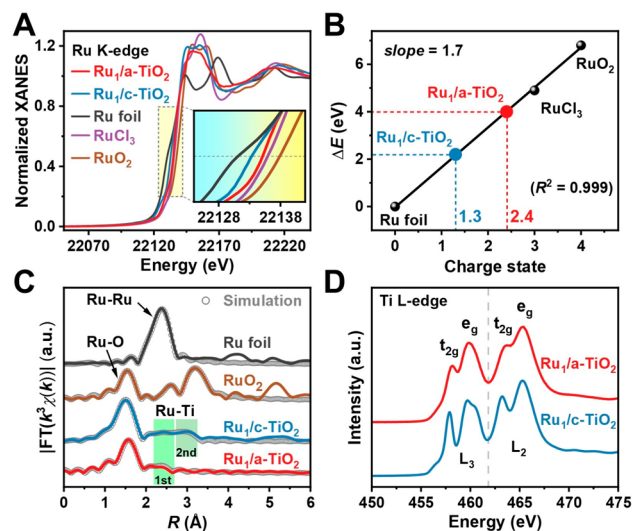


**Figure 2.** X-ray absorption spectrometric studies of Ru<sub>1</sub>/a-TiO<sub>2</sub> and Ru<sub>1</sub>/c-TiO<sub>2</sub>. (A) Ru K-edge XANES spectra. (B) Calculation of Ru charge states from Ru K-edge XANES. (C) Fourier transforms of Ru K-edge EXAFS and corresponding simulations. (D) Ti L-edge XANES spectra.

edge energies are linearly correlated to the charge states ( $\delta$ ) of Ru, a fit line based on standard samples (i.e., Ru foil, RuCl<sub>3</sub>, and RuO<sub>2</sub>) is obtained (Figures 2B and S9).<sup>24</sup> Thereby, the  $\delta$  values of Ru in Ru<sub>1</sub>/a-TiO<sub>2</sub> and Ru<sub>1</sub>/c-TiO<sub>2</sub> are calculated to be +2.4 and +1.3, respectively. These results are in line with the X-ray photoelectron spectroscopy (XPS) analyses (Figure S10). In the Fourier transforms (FTs) of the EXAFS spectra in *R* space (Figure 2C), the peak intensity for the first Ru–Ti shell of Ru<sub>1</sub>/a-TiO<sub>2</sub> is notably weak compared to Ru<sub>1</sub>/c-TiO<sub>2</sub>. Moreover, the signal for the second Ru–Ti shell of Ru<sub>1</sub>/a-TiO<sub>2</sub> is not observed. Further quantitative EXAFS fitting analysis (Figures 2C and S11) indicates that the average coordination number (*N*) in the Ru–Ti shell of Ru<sub>1</sub>/a-TiO<sub>2</sub> is 1.0, which is significantly less than that of Ru<sub>1</sub>/c-TiO<sub>2</sub> ( $N_{\text{first}} = 7.8$  and  $N_{\text{second}} = 4.2$ ) (Table S1). In the Ti L-edge XANES, the broad and weak peaks of Ru<sub>1</sub>/a-TiO<sub>2</sub> indicate the irregular distortions of *O<sub>h</sub>* symmetry at various directions and degrees (Figure 2D).<sup>25</sup> The resulting translational symmetry deficiency, which reduces the Ru–Ti interactions, is verified by the silent Raman modes (Figure S12).<sup>26,27</sup>

According to the experimental charge state and coordination environment, we calculated the atomic model of Ru<sub>1</sub>/a-TiO<sub>2</sub> by the constrained density functional theory (CDFT) method.<sup>28,29</sup> The details for the CDFT method are illustrated

in Scheme S1, and the calculation procedures are presented in Scheme S2 in the Supporting Information. In the DFT optimized  $\text{Ru}_1/\text{a-TiO}_2$  (Figure 3A), Ru is coordinated with

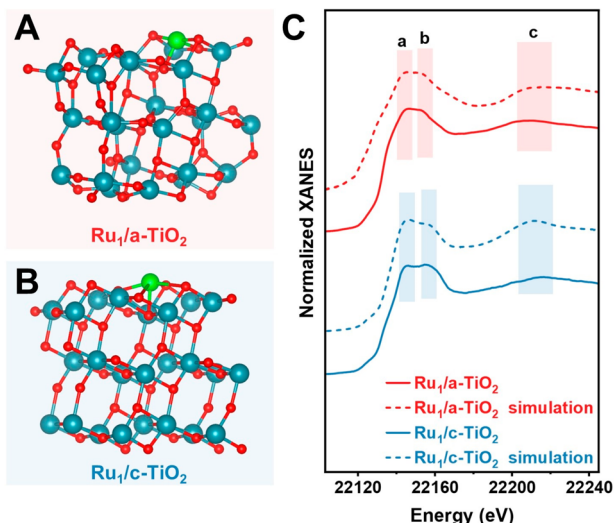


**Figure 3.** XANES simulations for the calculated structural models of  $\text{Ru}_1/\text{a-TiO}_2$  and  $\text{Ru}_1/\text{c-TiO}_2$ . (A,B) Calculated structural models of  $\text{Ru}_1/\text{a-TiO}_2$  and  $\text{Ru}_1/\text{c-TiO}_2$ . (C) Comparisons of the simulated and experimental XANES spectra. Atom colors: Ru, green; Ti, cyan; O, red.

four oxygen atoms ( $N_{\text{Ru-O}} = 4$ ), which is in accordance with the strong Ru–O shell signal in the FT-EXAFS of  $\text{Ru}_1/\text{a-TiO}_2$  (Figure 2C) and also close to the EXAFS fitting result ( $N_{\text{Ru-O}} = 4.2$ , Table S1). In addition, the first Ru–Ti shell ( $R = 2.5 \text{ \AA}$ ) of the DFT model shows a coordination number of  $N_{\text{Ru-Ti}} = 1$ , which agrees with the EXAFS analysis ( $N_{\text{Ru-Ti}} = 1.0$ , Table S1) that shows a weak band centered at  $R = 2.5 \text{ \AA}$  (Figure 2C). To further verify the calculated structure, XANES simulation was performed with the DFT model. As shown in Figure 3C, the simulated XANES spectrum using the  $\text{Ru}_1/\text{a-TiO}_2$  model agrees well with the characteristic peaks of the experimental XANES. Peak a is associated with the multiple back scattering from the 1s to 5p transition, and peak b is due to the single back scattering interferences between Ru and the neighboring atoms.<sup>30</sup> Due to the amorphous structure of the support, the Ru site has a disordered nearest-neighbor octahedral core. Meanwhile, the octahedral chains outside the core are less connected and progressively disordered.<sup>31</sup> Therefore, the white line region for peaks a and b of  $\text{Ru}_1/\text{a-TiO}_2$  is broadened and weakened compared to that of  $\text{Ru}_1/\text{c-TiO}_2$  (Figure 3B and C).

The experimental and theoretical analyses both indicate that the support amorphization could cause distinct geometric and electronic changes to single-atom Ru; thus, it is anticipated that the chemo-recognition behaviors of single-atom Ru will also be affected. Using a bifunctional molecule 4-nitrostyrene (NS) as the probe, we calculated the adsorption energies ( $E_{\text{ads}}$ ) of the nitro and vinyl groups on the catalyst surfaces. In the case of  $\text{Ru}_1/\text{c-TiO}_2$ , the adsorption capacity for the vinyl group ( $E_{\text{ads}} = 2.7 \text{ eV}$ ) is stronger than that of the nitro group ( $E_{\text{ads}} = 1.6 \text{ eV}$ ) (Figure 4A, left), indicating the adsorption configuration  $-\text{CH}=\text{CH}_2@Ru$  is favored on  $\text{Ru}_1/\text{c-TiO}_2$ . However, in the case of  $\text{Ru}_1/\text{a-TiO}_2$ , an opposite adsorption configuration  $-\text{NO}_2@Ru$  is favored, as the adsorption strength for the nitro group ( $E_{\text{ads}} = 3.2 \text{ eV}$ ) is higher than that of the vinyl group ( $E_{\text{ads}} = 2.6 \text{ eV}$ ) on  $\text{Ru}_1/\text{a-TiO}_2$  (Figure 4B, left).

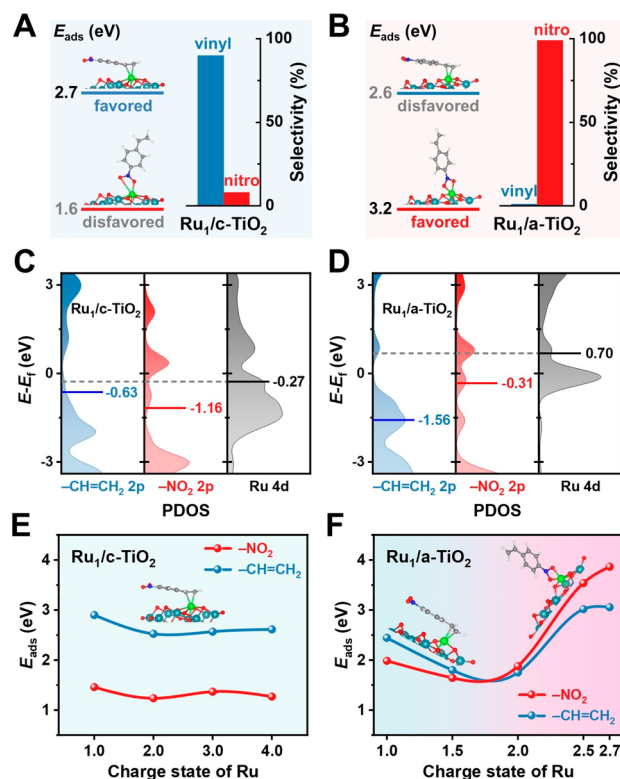


**Figure 4.** Experimental and theoretical analyses for selectivities of  $\text{Ru}_1/\text{a-TiO}_2$  and  $\text{Ru}_1/\text{c-TiO}_2$ . (A,B) Catalytic selectivities at half conversion of 4-nitrostyrene and calculated adsorption energies for different adsorption configurations. Reaction conditions: 4-nitrostyrene (0.1 mmol),  $\text{Ru}_1/\text{a-TiO}_2$  (0.6 mol % based on Ru), 1,4-dioxane (10 mL),  $\text{H}_2$  (2 MPa), 343 K. (C,D) Band center analyses of nitro N and O 2p, vinyl C 2p, and Ru 4d orbitals for adsorption of 4-nitrostyrene on catalysts. (E,F) Correlations between adsorption energies and charge states of Ru. Atom colors: Ru, green; Ti, cyan; O, red; C, black; H, white.

As a proof-of-concept demonstration, the catalytic selective hydrogenation reactions of NS were conducted using the as-prepared catalysts. According to the reaction pathways (Figure S13), at half conversion of NS, the hydrogenation product 4-aminostyrene (AS) reflects the nitro selectivity, while 4-ethylnitrobenzene (EN) reveals the vinyl selectivity.<sup>32</sup> As a result,  $\text{Ru}_1/\text{a-TiO}_2$  demonstrates an opposite hydrogenation selectivity in comparison with  $\text{Ru}_1/\text{c-TiO}_2$ . At half conversion of NS,  $\text{Ru}_1/\text{c-TiO}_2$  exhibits 90% vinyl selectivity (Figure 4A, right), whereas  $\text{Ru}_1/\text{a-TiO}_2$  demonstrates 99% nitro selectivity (Figure 4B, right). The high nitro selectivity of  $\text{Ru}_1/\text{a-TiO}_2$  could be retained after five cycles (Figure S14). Meanwhile, the amorphous characteristic of  $\text{Ru}_1/\text{a-TiO}_2$  after the cycling test was verified to be intact by PXRD analysis (Figure S15). The heterogeneous catalytic feature of  $\text{Ru}_1/\text{a-TiO}_2$  was confirmed by a leaching test (Figure S16). The ICP-OES analysis for the postreaction catalysts indicates that the Ru species could be well retained rather than leached out during the reaction (Figures S17 and S18). The high catalytic activity of  $\text{Ru}_1/\text{a-TiO}_2$  was further demonstrated with a high substrate/catalyst ratio ( $S/C = 1000$ ), affording 96% conversion with 94% nitro selectivity (Table S2).  $\text{Ru}_1/\text{a-TiO}_2$  was also examined with other substituted nitrobenzenes in the selective hydrogenation reactions, and it exhibited a high tolerance for a range of functional groups, such as aldehyde, chloride, and cyano groups (Table S3).



To shed light on the nitro selectivity of Ru<sub>1</sub>/a-TiO<sub>2</sub>, opposite to the vinyl selectivity of Ru<sub>1</sub>/c-TiO<sub>2</sub>, band center analyses for the orbitals of functional groups and single-atom Ru were performed. For Ru<sub>1</sub>/c-TiO<sub>2</sub>, the partial density of states (PDOS) near the Fermi level ( $E_f$ ) shows that the Ru d-band center (−0.27 eV) is close to the vinyl C p-band center (−0.63 eV) but far away from the nitro N and O p-band center (−1.16 eV) (Figure 4C). It indicates that the coupling of the Ru 4d orbitals with the nitro 2p orbitals is weaker than that with the vinyl 2p orbitals. In contrast, a very different trend is found in the amorphous structure. For Ru<sub>1</sub>/a-TiO<sub>2</sub>, the Ru d-band center (0.70 eV) is close to the nitro N and O p-band center (−0.31 eV) and far away from the vinyl p-band center (−1.56 eV) (Figure 4D), indicating that the Ru active single sites on the amorphous support are more inclined to interact with the nitro group compared to the vinyl group.

We then move further to evaluate the geometric and electronic effects on single-atom Ru by the support through constraining the Ru charge state on different TiO<sub>2</sub> phase via CDFT method.<sup>33,34</sup> As shown in Figure 4E, for Ru<sub>1</sub>/c-TiO<sub>2</sub>,  $E_{\text{ads}}$  of both  $-\text{CH}=\text{CH}_2\text{@Ru}$  and  $-\text{NO}_2\text{@Ru}$  are slightly affected by the charge states of the metal center but the former is higher than the latter at the full range of  $\delta$  values (Table S4). It indicates that the crystalline support, rather than the charge states of Ru, is responsible for the vinyl selectivity. However, in the amorphous support, the charge states of Ru could significantly affect the adsorption strength of the nitro group, while the effect on the vinyl group is relatively weak (Figure 4F). With the increase of the charge state of Ru,  $E_{\text{ads}}$  of  $-\text{NO}_2\text{@Ru}$  gradually surpasses that of  $-\text{CH}=\text{CH}_2\text{@Ru}$  (Table S5), and this trend eventually causes the reversal of chemo-recognition and leads to the nitro selectivity of Ru<sub>1</sub>/a-TiO<sub>2</sub> in the hydrogenation reaction. Additionally, the calculations on the whole hydrogenation processes indicate that the reaction could proceed in different pathways, i.e., vinyl hydrogenation for Ru<sub>1</sub>/c-TiO<sub>2</sub> (Figure S19, Tables S6 and S7) and nitro hydrogenation for Ru<sub>1</sub>/a-TiO<sub>2</sub> (Figure S20, Tables S8 and S9).

In summary, we reported the phase engineering of support for single-atom Ru to control its catalytic selectivity in hydrogenation process. Single-atom Ru on amorphous TiO<sub>2</sub> porous ultrathin nanosheets, Ru<sub>1</sub>/a-TiO<sub>2</sub>, was synthesized, exhibiting a more positive charge state of Ru compared to that in its crystalline counterpart, Ru<sub>1</sub>/c-TiO<sub>2</sub>. The favored adsorption configuration of 4-nitrostyrene is  $-\text{CH}=\text{CH}_2\text{@Ru}$  on Ru<sub>1</sub>/c-TiO<sub>2</sub>, but it could be inverted to  $-\text{NO}_2\text{@Ru}$  on Ru<sub>1</sub>/a-TiO<sub>2</sub>. Thus, in the hydrogenation process, a superior nitro selectivity (99%) was achieved by Ru<sub>1</sub>/a-TiO<sub>2</sub>, opposite to the vinyl selectivity of Ru<sub>1</sub>/c-TiO<sub>2</sub>, illustrating the key role of the support phase in heterogeneous single-atom catalysis. Since the amorphous phase exists widely in materials and could potentially be employed in the supported metal catalysts, this work will attract broad interest in phase engineering for advanced catalysis.

## EXPERIMENTAL SECTION

### Chemicals

All chemicals were used as received without further purification. Potassium bromide (KBr), dichloromethane (DCM), 1,4-dioxane, and alcohol were purchased from Sinopharm Chemical Reagent Co., Ltd. Titanium acetylacetonate (Ti(acac)<sub>3</sub>, ca. 63% in isopropyl alcohol) and 4-nitrostyrene were purchased from TCI. Ruthenium acetylacetonate (Ru(acac)<sub>3</sub>) was supplied by Adamas-beta. Deionized

(DI) water from Milli-Q System (Millipore, Billerica, MA) was used in all our experiments.

### Preparation of Ru<sub>1</sub>/a-TiO<sub>2</sub>

In a typical synthesis, 400 mg of KBr was finely crushed and vigorously ground in a mortar. Meanwhile, 100  $\mu\text{L}$  of Ti(acac)<sub>3</sub> and 0.74 mg of Ru(acac)<sub>3</sub> were dissolved in 5 mL of DCM and treated with ultrasound for 0.5 h. Then the mixture was transferred into the mortar and ground together with the KBr powder until dry to achieve uniformity. Subsequently, the obtained powder mixture was placed in a ceramic boat at the center temperature zone and then heated to 300 °C at 5 °C/min and kept for 2 h under air in a tube furnace. After cooling to room temperature, the product was washed with water and ethanol several times. Finally, the as-prepared Ru<sub>1</sub>/a-TiO<sub>2</sub> was freeze-dried under vacuum for further use and characterization. The Ru-free sample a-TiO<sub>2</sub> was prepared by the same procedure without Ru(acac)<sub>3</sub>.

### Preparation of Ru<sub>1</sub>/c-TiO<sub>2</sub>

The powder of Ru<sub>1</sub>/a-TiO<sub>2</sub> was placed in a ceramic boat at the center temperature zone and then heated to 450 °C at 5 °C/min and kept for 1 h under air in a tube furnace. After cooling to room temperature, the as-prepared Ru<sub>1</sub>/c-TiO<sub>2</sub> was collected for further use and characterization.

### Catalytic Reaction

The catalytic reactions were carried out in a Wattcas Schlenk autoclave equipped with a high-pressure sampling system with needle valve. A magnetic stirrer was used to facilitate the mass transfer. In a typical test, the substrate (0.1 mmol) and catalyst (0.6 mol % based on Ru) in 10 mL of 1,4-dioxane were added in the reactor. After washing the reactor with H<sub>2</sub> three times, the pressure was adjusted to 2 MPa and the reaction was allowed to proceed at 343 K. The progress of the reaction was monitored by gas chromatography–mass spectrometry (Agilent 7890A/5975C GC-MS system with an HP-5 MS column).

### Leaching Test

Before the leaching test, a typical catalytic reaction was allowed to proceed for 2 h, and GC-MS shows that the conversion reached 54%. Afterward, the reaction mixture was divided into two equal portions, denoted as A and B. The catalyst in A was removed by centrifugation, while B remained untouched. Then, the reactions of A and B were allowed to continue, respectively, and the reaction processes were monitored by GC-MS. After an additional 1.5 h, the conversion in B reached 99% while the conversion in A barely increased, indicating that Ru<sub>1</sub>/a-TiO<sub>2</sub> is indeed a heterogeneous catalyst.

### Recycling Test

The recycling performance of Ru<sub>1</sub>/a-TiO<sub>2</sub> was evaluated in a five-run recycling test. After each run, the catalyst was recovered by centrifugation, washed with ethanol several times to remove the organic residue, dried in vacuum, and then charged into the next run. Although the full conversion could be achieved by prolonging the reaction time, for better illustration of the catalytic activity and selectivity, each run was stopped after 2 h to evaluate the recycling performance.

## ASSOCIATED CONTENT

### Supporting Information

The Supporting Information is available free of charge at <https://pubs.acs.org/doi/10.1021/jacsau.2c00192>.

Experimental and computational details and characterization methods; SEM, TEM, AFM, N<sub>2</sub> sorption, Raman, PXRD, XPS, and EXAFS data (PDF)

## ■ AUTHOR INFORMATION

## Corresponding Authors

**Jun Jiang** – Center of Advanced Nanocatalysis (CAN), Department of Applied Chemistry, University of Science and Technology of China, Hefei 230026, P. R. China; [orcid.org/0000-0002-6116-5605](https://orcid.org/0000-0002-6116-5605); Email: [jiangj1@ustc.edu.cn](mailto:jiangj1@ustc.edu.cn)

**Xun Hong** – Center of Advanced Nanocatalysis (CAN), Department of Applied Chemistry, University of Science and Technology of China, Hefei 230026, P. R. China; [orcid.org/0000-0003-2784-2868](https://orcid.org/0000-0003-2784-2868); Email: [hongxun@ustc.edu.cn](mailto:hongxun@ustc.edu.cn)

## Authors

**Junyi Du** – Center of Advanced Nanocatalysis (CAN), Department of Applied Chemistry, University of Science and Technology of China, Hefei 230026, P. R. China; Division of Advanced Materials, Suzhou Institute of Nano-Tech and Nano-Bionics, Chinese Academy of Sciences, Suzhou 215123, P. R. China; [orcid.org/0000-0001-6234-4405](https://orcid.org/0000-0001-6234-4405)

**Yan Huang** – Center of Advanced Nanocatalysis (CAN), Department of Applied Chemistry, University of Science and Technology of China, Hefei 230026, P. R. China

**Zixiang Huang** – Center of Advanced Nanocatalysis (CAN), Department of Applied Chemistry, University of Science and Technology of China, Hefei 230026, P. R. China; National Synchrotron Radiation Laboratory (NSRL), University of Science and Technology of China, Hefei 230029, P. R. China

**Geng Wu** – Center of Advanced Nanocatalysis (CAN), Department of Applied Chemistry, University of Science and Technology of China, Hefei 230026, P. R. China

**Bei Wu** – Center of Advanced Nanocatalysis (CAN), Department of Applied Chemistry, University of Science and Technology of China, Hefei 230026, P. R. China

**Xiao Han** – Center of Advanced Nanocatalysis (CAN), Department of Applied Chemistry, University of Science and Technology of China, Hefei 230026, P. R. China

**Cai Chen** – Center of Advanced Nanocatalysis (CAN), Department of Applied Chemistry, University of Science and Technology of China, Hefei 230026, P. R. China

**Xusheng Zheng** – National Synchrotron Radiation Laboratory (NSRL), University of Science and Technology of China, Hefei 230029, P. R. China

**Peixin Cui** – Key Laboratory of Soil Environment and Pollution Remediation, Institute of Soil Science, Chinese Academy of Sciences, Nanjing 210008, P. R. China; [orcid.org/0000-0002-9887-2784](https://orcid.org/0000-0002-9887-2784)

**Yuen Wu** – Center of Advanced Nanocatalysis (CAN), Department of Applied Chemistry, University of Science and Technology of China, Hefei 230026, P. R. China; [orcid.org/0000-0001-9524-2843](https://orcid.org/0000-0001-9524-2843)

Complete contact information is available at: <https://pubs.acs.org/10.1021/jacsau.2c00192>

## Author Contributions

<sup>†</sup>J.D., Y.H., and Z.H. contributed equally.

## Notes

The authors declare no competing financial interest.

## ■ ACKNOWLEDGMENTS

This work was supported by the National Key R&D Program of China (2017YFA0700104, 2018YFA0702001), National Natural Science Foundation of China (21871238, 22025304, 22033007), China Postdoctoral Science Foundation (2019M662163), Youth Innovation Promotion Association of Chinese Academy of Sciences (2018494), and Fundamental Research Funds for the Central Universities (WK2060000016). The theoretical calculations are supported by the Supercomputing Center of University of Science and Technology of China. We thank the photoemission endstations BL14W1 in Shanghai Synchrotron Radiation Facility (SSRF), BL10B and BL11U in National Synchrotron Radiation Laboratory (NSRL) for the help in characterizations.

## ■ REFERENCES

- (1) Lu, Y.; Liu, T.; Dong, C. L.; Huang, Y. C.; Li, Y.; Chen, J.; Zou, Y.; Wang, S. Tuning the Selective Adsorption Site of Biomass on  $\text{Co}_3\text{O}_4$  by Ir Single Atoms for Electrosynthesis. *Adv. Mater.* **2021**, 33, 2007056.
- (2) He, X.; He, Q.; Deng, Y.; Peng, M.; Chen, H.; Zhang, Y.; Yao, S.; Zhang, M.; Xiao, D.; Ma, D.; Ge, B.; Ji, H. A Versatile Route To Fabricate Single Atom Catalysts with High Chemoselectivity and Regioselectivity in Hydrogenation. *Nat. Commun.* **2019**, 10, 3663.
- (3) Huang, F.; Deng, Y.; Chen, Y.; Cai, X.; Peng, M.; Jia, Z.; Xie, J.; Xiao, D.; Wen, X.; Wang, N.; Jiang, Z.; Liu, H.; Ma, D. Anchoring  $\text{Cu}_1$  Species over Nanodiamond-Graphene for Semi-Hydrogenation of Acetylene. *Nat. Commun.* **2019**, 10, 4431.
- (4) Jagadeesh, R. V.; Surkus, A.-E.; Junge, H.; Pohl, M.-M.; Radnik, J.; Rabeah, J.; Huan, H.; Schünemann, V.; Brückner, A.; Beller, M. Nanoscale  $\text{Fe}_2\text{O}_3$ -based catalysts for selective hydrogenation of nitroarenes to anilines. *Science* **2013**, 342, 1073–1076.
- (5) Liu, H.; Li, X.; Ma, Z.; Sun, M.; Li, M.; Zhang, Z.; Zhang, L.; Tang, Z.; Yao, Y.; Huang, B.; Guo, S. Atomically Dispersed Cu Catalyst for Efficient Chemoselective Hydrogenation Reaction. *Nano Lett.* **2021**, 21, 10284–10291.
- (6) Cheong, W. C.; Yang, W.; Zhang, J.; Li, Y.; Zhao, D.; Liu, S.; Wu, K.; Liu, Q.; Zhang, C.; Wang, D.; Peng, Q.; Chen, C.; Li, Y. Isolated Iron Single-Atomic Site-Catalyzed Chemoselective Transfer Hydrogenation of Nitroarenes to Arylamines. *ACS Appl. Interfaces* **2019**, 11, 33819–33824.
- (7) Meng, X.; Yang, Y.; Chen, L.; Xu, M.; Zhang, X.; Wei, M. A Control over Hydrogenation Selectivity of Furfural via Tuning Exposed Facet of Ni Catalysts. *ACS Catal.* **2019**, 9, 4226–4235.
- (8) Furukawa, S.; Takahashi, K.; Komatsu, T. Well-Structured Bimetallic Surface Capable of Molecular Recognition for Chemoselective Nitroarene Hydrogenation. *Chem. Sci.* **2016**, 7, 4476–4484.
- (9) Mao, J.; Chen, W.; Sun, W.; Chen, Z.; Pei, J.; He, D.; Lv, C.; Wang, D.; Li, Y. Rational Control of the Selectivity of a Ruthenium Catalyst for Hydrogenation of 4-Nitrostyrene by Strain Regulation. *Angew. Chem., Int. Ed.* **2017**, 56, 11971–11975.
- (10) Du, X.; Huang, Y.; Pan, X.; Han, B.; Su, Y.; Jiang, Q.; Li, M.; Tang, H.; Li, G.; Qiao, B. Size-Dependent Strong Metal-Support Interaction in  $\text{TiO}_2$  Supported Au Nanocatalysts. *Nat. Commun.* **2020**, 11, 5811.
- (11) Goyal, R.; Sarkar, B.; Bag, A.; Siddiqui, N.; Dumbre, D.; Lucas, N.; Bhargava, S. K.; Bordoloi, A. Studies of Synergy Between Metal-Support Interfaces and Selective Hydrogenation of HMF to DMF in Water. *J. Catal.* **2016**, 340, 248–260.
- (12) Wu, W.; Li, J.; Chen, Z.; Chen, W.; Pang, H.; Ma, K.; Zeng, J. High-Index Facets of Pt-Fe Nanowires Induce Steric Effect on Selective Hydrogenation of Acetophenone. *J. Catal.* **2019**, 373, 209–214.
- (13) Zhang, L.; Zhou, M.; Wang, A.; Zhang, T. Selective Hydrogenation over Supported Metal Catalysts: From Nanoparticles to Single Atoms. *Chem. Rev.* **2020**, 120, 683–733.

- (14) Ge, J.; He, D.; Chen, W.; Ju, H.; Zhang, H.; Chao, T.; Wang, X.; You, R.; Lin, Y.; Wang, Y.; Zhu, J.; Li, H.; Xiao, B.; Huang, W.; Wu, Y.; Hong, X.; Li, Y. Atomically Dispersed Ru on Ultrathin Pd Nanoribbons. *J. Am. Chem. Soc.* **2016**, *138*, 13850–13853.
- (15) Li, S.; Dong, M.; Yang, J.; Cheng, X.; Shen, X.; Liu, S.; Wang, Z. Q.; Gong, X. Q.; Liu, H.; Han, B. Selective Hydrogenation of 5-(Hydroxymethyl)furfural to 5-Methylfurfural over Single Atomic Metals Anchored On Nb<sub>2</sub>O<sub>5</sub>. *Nat. Commun.* **2021**, *12*, 584.
- (16) Campbell, C. T. Catalyst-Support Interactions: Electronic Perturbations. *Nat. Chem.* **2012**, *4*, 597–598.
- (17) Li, J.; Guan, Q.; Wu, H.; Liu, W.; Lin, Y.; Sun, Z.; Ye, X.; Zheng, X.; Pan, H.; Zhu, J.; Chen, S.; Zhang, W.; Wei, S.; Lu, J. Highly Active and Stable Metal Single-Atom Catalysts Achieved by Strong Electronic Metal-Support Interactions. *J. Am. Chem. Soc.* **2019**, *141*, 14515–14519.
- (18) Shin, S.; Haaring, R.; So, J.; Choi, Y.; Lee, H. Highly Durable Heterogeneous Atomic Catalysts. *Acc. Chem. Res.* **2022**, DOI: 10.1021/acs.accounts.1c00734.
- (19) Yang, J.; Li, W.; Wang, D.; Li, Y. Electronic Metal-Support Interaction of Single-Atom Catalysts and Applications in Electrocatalysis. *Adv. Mater.* **2020**, *32*, 2003300.
- (20) Shi, Y.; Ma, Z. R.; Xiao, Y. Y.; Yin, Y. C.; Huang, W. M.; Huang, Z. C.; Zheng, Y. Z.; Mu, F. Y.; Huang, R.; Shi, G. Y.; Sun, Y. Y.; Xia, X. H.; Chen, W. Electronic Metal-Support Interaction Modulates Single-Atom Platinum Catalysis for Hydrogen Evolution Reaction. *Nat. Commun.* **2021**, *12*, 3021.
- (21) Yang, J.; Li, W. H.; Tan, S.; Xu, K.; Wang, Y.; Wang, D.; Li, Y. The Electronic Metal-Support Interaction Directing the Design of Single Atomic Site Catalysts: Achieving High Efficiency Towards Hydrogen Evolution. *Angew. Chem., Int. Ed.* **2021**, *60*, 19085–19091.
- (22) Lin, Z.; Du, C.; Yan, B.; Wang, C.; Yang, G. Two-Dimensional Amorphous NiO as a Plasmonic Photocatalyst for Solar H<sub>2</sub> Evolution. *Nat. Commun.* **2018**, *9*, 4036.
- (23) Wu, G.; Zheng, X.; Cui, P.; Jiang, H.; Wang, X.; Qu, Y.; Chen, W.; Lin, Y.; Li, H.; Han, X.; Hu, Y.; Liu, P.; Zhang, Q.; Ge, J.; Yao, Y.; Sun, R.; Wu, Y.; Gu, L.; Hong, X.; Li, Y. A General Synthesis Approach for Amorphous Noble Metal Nanosheets. *Nat. Commun.* **2019**, *10*, 4855.
- (24) Li, Q.; Chen, W.; Xiao, H.; Gong, Y.; Li, Z.; Zheng, L.; Zheng, X.; Yan, W.; Cheong, W.-C.; Shen, R.; Fu, N.; Gu, L.; Zhuang, Z.; Chen, C.; Wang, D.; Peng, Q.; Li, J.; Li, Y. Fe Isolated Single Atoms on S, N Codoped Carbon by Copolymer Pyrolysis Strategy for Highly Efficient Oxygen Reduction Reaction. *Adv. Mater.* **2018**, *30*, 1800588.
- (25) Kroll, T.; Solomon, E. I.; de Groot, F. M. Final-State Projection Method in Charge-Transfer Multiplet Calculations: An Analysis of Ti L-Edge Absorption Spectra. *J. Phys. Chem. B* **2015**, *119*, 13852–13858.
- (26) Ohsaka, T.; Izumi, F.; Fujiki, Y. Raman Spectrum of Anatase, TiO<sub>2</sub>. *J. Raman Spectrosc.* **1978**, *7*, 321–324.
- (27) Zhang, Y.; Wu, W.; Zhang, K.; Liu, C.; Yu, A.; Peng, M.; Zhai, J. Raman Study of 2D Anatase TiO<sub>2</sub> Nanosheets. *Phys. Chem. Chem. Phys.* **2016**, *18*, 32178–32184.
- (28) Kaduk, B.; Kowalczyk, T.; Van Voorhis, T. Constrained Density Functional Theory. *Chem. Rev.* **2012**, *112*, 321–370.
- (29) Wang, X.; Shi, W.; Wang, S.; Zhao, H.; Lin, J.; Yang, Z.; Chen, M.; Guo, L. Two-Dimensional Amorphous TiO<sub>2</sub> Nanosheets Enabling High-Efficiency Photoinduced Charge Transfer for Excellent SERS Activity. *J. Am. Chem. Soc.* **2019**, *141*, 5856–5862.
- (30) Kim, J.; Shih, P.-C.; Tsao, K.-C.; Pan, Y.-T.; Yin, X.; Sun, C.-J.; Yang, H. High-Performance Pyrochlore-Type Yttrium Ruthenate Electrocatalyst for Oxygen Evolution Reaction in Acidic Media. *J. Am. Chem. Soc.* **2017**, *139*, 12076–12083.
- (31) McKeown, D. A.; Hagans, P. L.; Carrette, L. P. L.; Russell, A. E.; Swider, K. E.; Rolison, D. R. Structure of Hydrated Ruthenium Oxides: Implications for Charge Storage. *J. Phys. Chem. B* **1999**, *103*, 4825–4832.
- (32) Macino, M.; Barnes, A. J.; Althahban, S. M.; Qu, R.; Gibson, E. K.; Morgan, D. J.; Freakley, S. J.; Dimitratos, N.; Kiely, C. J.; Gao, X.; Beale, A. M.; Bethell, D.; He, Q.; Sankar, M.; Hutchings, G. J. Tuning of Catalytic Sites in Pt/TiO<sub>2</sub> Catalysts for the Chemoselective Hydrogenation of 3-Nitrostyrene. *Nat. Catal.* **2019**, *2*, 873–881.
- (33) Zhong, W.; Zhang, G.; Zhang, Y.; Jia, C.; Yang, T.; Ji, S.; Prezhd, O. V.; Yuan, J.; Luo, Y.; Jiang, J. Enhanced Activity of C<sub>2</sub>N-Supported Single Co Atom Catalyst by Single Atom Promoter. *J. Phys. Chem. Lett.* **2019**, *10*, 7009–7014.
- (34) Ku, C.; Sit, P. H. Oxidation-State Constrained Density Functional Theory for the Study of Electron-Transfer Reactions. *J. Chem. Theory Comput.* **2019**, *15*, 4781–4789.